Mechanical design and modeling of a single-piston pump for the novel power take-off system of a wave energy converter

Vakis, Antonis I.; Anagnostopoulos, John S.

Published in:
Renewable Energy

DOI:
10.1016/j.renene.2016.04.076

Renewable Energy 96 (2016) 531–547

Contents lists available at ScienceDirect

Renewable Energy

journal homepage: www.elsevier.com/locate/renene

Mechanical design and modeling of a single-piston pump for the novel power take-off system of a wave energy converter

Antonis I. Vakis [a, *], John S. Anagnostopoulos [b]

[a] Advanced Production Engineering, Engineering and Technology Institute Groningen, Faculty of Mathematics & Natural Sciences, University of Groningen, Nijenborgh 4, Groningen 9747AG, The Netherlands
[b] Fluids Section, Laboratory of Hydraulic Turbomachines, School of Mechanical Engineering, National Technical University of Athens, 9 Heroon Polytechniou, Zografou, 15780, Athens, Greece

ARTICLE INFO

Article history:
Received 20 January 2015
Received in revised form
14 March 2016
Accepted 24 April 2016
Available online 13 May 2016

Keywords:
Wave energy harvesters
Mechanical design
Elastohydrodynamic lubrication
Fluid mechanics
Simulation model

ABSTRACT

A multi-pump, multi-piston power take-off wave energy converter (MP^{2}PTO WEC) has been proposed for use with a novel renewable energy harvester termed the Ocean Grazer. The MP^{2}PTO WEC utilizes wave motion to pump—via buoys connected to pistons—working fluid within a closed circuit and store it as potential energy that can be converted to electricity via turbines. This paper introduces the mechanical design and model-based performance prediction of a single-piston pump that constitutes the basic building block for the MP^{2}PTO WEC. Results provide preliminary validation of aqueous lubrication as a viable means of reducing friction and wear, suggesting that water-based hydraulic fluids can prohibit solid contact at the piston-cylinder interface while reducing volumetric leakage, and allowing for an estimation of the energy extraction efficiency for the mechanical pumping system. Pending more thorough and extended tribological investigations using the methodology introduced in this paper, findings suggest that the overall system efficiency will be dictated by the hydrodynamics of the buoys actuating the pumping system.

1. Introduction

A number of near- and off-shore wave energy converters (WECs) have been proposed in recent years based on attenuator [1,2], point absorber [3], overtopping [4], and other design principles; for a comprehensive review of existing WEC technologies, the reader is referred to a recent report published by the Strategic Initiative for Ocean Energy [5]. In an effort to improve on the state-of-the-art, the University of Groningen has patented a novel semi-submersible renewable energy harvester, termed the *Ocean Grazer*, with a *multi-pump, multi-piston power take-off (MP^{2}PTO)* WEC at its core. A single Ocean Grazer device, for which the MP^{2}PTO WEC employing multiple multi-piston pump units will contribute about 80% of power generation (secondary technologies such as oscillating water column and wind turbine systems will contribute the rest), is projected to produce more than 200 GWh/year and have a storage capacity of about 800 MWh [6,7].

The operating principle of the MP^{2}PTO WEC, shown in Fig. 1(a), is to create pressure difference (hydraulic head, H) in the working fluid circulating between two reservoirs that can be transformed into electricity via a turbine (T). A modified point absorber design will be used such that floating buoys (B_i) will follow the motion of an incident wave and actuate linear hydraulic pumps (P_i) to move the working fluid column during the upstroke. In this manner, the working fluid can be pumped to the upper reservoir where it will be stored as lossless potential energy, and allowing for the decoupling of electricity generation from the variability of available wave energy over timescales of seconds (for individual waves) to hours and days.

Varying sea conditions determine an incident wave's characteristics such that each wave may differ significantly from those preceding or following it; ideally, a WEC should be able to extract energy from both small and large waves with a range of periods. Energy extraction is expected to diminish the energy content and height of a wave as it moves through a WEC. In the case of the Ocean Grazer, which will employ a grid of buoys – termed a *floater blanket* – to actuate the pumps, the first pump unit can potentially extract more energy than the second, and so on. To account for the inherent variability in wave energy content, multiple pistons will

* Corresponding author.
E-mail addresses: a.vakis@rug.nl (A.I. Vakis), anagno@fluid.mech.ntua.gr (J.S. Anagnostopoulos).

http://dx.doi.org/10.1016/j.renene.2016.04.076

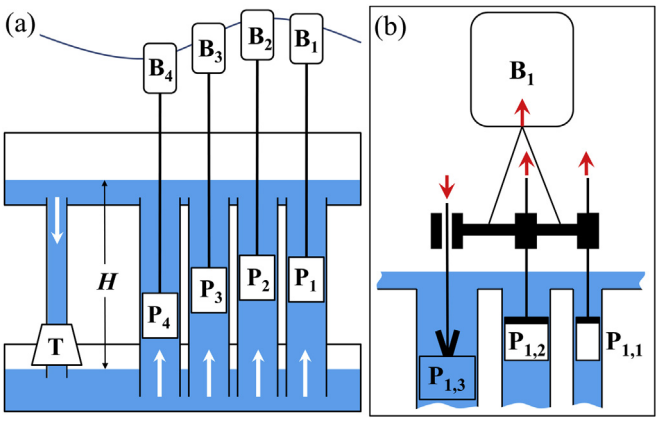

Fig. 1. The MP^{2}PTO WEC (a) and multi-piston pump (b).

be activated within each pump in the Ocean Grazer, as shown in Fig. 1(b), to maximize energy extraction for waves ranging in height from 1 to 12 m and periods of 4 to 20 s [6,7]: controlling the coupling between any buoy (B_i) and a number of variable-size pistons ($P_{i,j}$) can optimize the load the buoy has to carry to achieve resonance during the upstroke and let an uncoupled piston sink due to its own weight during the downstroke. Preliminary work has demonstrated the successful potential use of variable-load control for a multi-piston pump [8]; however, the focus of the present work is the tribological characterization of the behavior of a single-piston pump unit – that will constitute the basic building block for the multi-piston and, eventually, the MP^{2}PTO WEC – in order to better understand the dynamic behavior of the piston based on physics-based formulations of the forces and pressures acting on it. While variable-load control is not discussed within the context of the present model, this work will be essential in the future design and implementation of improved control schemes [9]. Similarly, previously developed methodologies for a hydro-pumped storage system utilizing a number of pumps in parallel operation will be useful in the eventual transition from a single-to a multi-pump system [10,11].

The main tribological interfaces of interest in the MP^{2}PTO WEC are between the piston and cylinder and at the seals that isolate the working fluid from sea water while allowing for the cable connections to transfer the buoy motion to the pistons. While the sealing problem is important because of sea water's highly corrosive and biofouling attributes, it is not addressed in the current work. Instead, it is assumed that perfect sealing is achieved so that the working fluid circulation is completely isolated from sea water, while buoy motion is transferred without frictional losses to the piston via a cable or rod of known stiffness. Future research on the tribology of the cable-seal interface will allow for the relaxation of these assumptions, especially within the context of flexible diamond-like carbon coatings that can be used in rubber seals [12]. Flexible coatings will also be relevant in secondary tribological interfaces between the piston and piston flaps as well as the one-way valves preventing working fluid backflow.

Scaling and maintenance issues require the design and use of a robust and abundant lubricant supply to the tribological interfaces. This suggests that a water-based hydraulic fluid optimized for the operating conditions of the piston-cylinder interface could potentially be used as a lubricant. Aqueous lubrication [13] was initially investigated within the context of environmental humidity at tribological interfaces [14], and subsequently for use with polymer composite coatings [15–17], and ceramic coatings with [18] and without texturing [19]. As a starting point, the present work assumes that a water-based hydraulic fluid (e.g. ISO Class HFC, a watery polymer solution) is used as the working fluid, while thermal effects are neglected at the piston-cylinder interface, where elastohydrodynamic (EHL) lubrication regimes are expected. Similarly to reciprocating engines [20], Sterling engines [21] and ring-less compressors [22], piston motion could result in boundary lubrication when the relative velocity at the interface becomes close to zero (at the top- and bottom-dead-centers), while EHL can be maintained otherwise. One of the questions to be answered with this work is whether EHL can be maintained throughout the piston stroke. Focusing on the piston-cylinder interface, the present model adopts existing methodologies to analyze the incompressible, inviscid and isothermal EHL problem. Future work will investigate the potential inclusion of piston rings, which may reduce working fluid backflow but increase friction, thereby complicating the lubrication issue.

A two-degree-of-freedom (2DOF) dynamical model comprising switching-state (upward versus downward motion), second order equations with an external forcing function was formulated in previous work [7,8]. This did not include friction and simplified the lubrication regime at the piston-cylinder interface by assuming hydrodynamic (Couette) flow. The current model builds on this dynamical model by adding EHL and solid contact and friction forces at the piston-cylinder interface based on solutions of the EHL problem. Further improvements to the model are planned in future work, including the formulation of realistic (irregular) wave displacement profiles serving as the external excitation, and accounting for the loss of wave energy content (and height) in the downstream direction due to energy extraction relevant for the MP^{2}PTO WEC; the inclusion of additional degrees of freedom for the piston and the buoy, such as downstream translation depending on buoy hydrodynamics; and, the improved modeling of dynamical piston behavior including piston flap (valve) dynamics and the drag force acting on the piston during sinking within the fluid column as a function of piston design.

The overall efficiency of the Ocean Grazer will depend on frictional and hydrodynamic energy losses at the MP^{2}PTO WEC. Therefore, minimizing friction and understanding the hydrodynamic behavior of grids of buoys are of paramount importance to maximize wave energy extraction as is reducing wear to ensure robust operation with little need for maintenance, especially in the presence of multiple tribological interfaces. Our results show that volumetric leakage at the piston-cylinder separation is critical in determining the overall pumping efficiency: this will decrease to below 80% for piston-cylinder separations larger than 200 μm, a finding that agrees with computational fluid dynamics simulations [23], pointing to target piston-cylinder separations around 100 μm when pure water is used as a lubricant. Such separations are comparable to those used in relevant applications such as ringless compressors, diesel and Sterling engines with typical values of 10 μm, 63 μm and 500 μm, respectively, and their optimization will be the focus of future work [20–22]. The present model is the first step in validating the pumping system's mechanical efficiency that has been measured in a small-scale prototype to be close to 99% and, hence, the potential of the Ocean Grazer to becoming a viable renewable energy harvester.

2. Dynamical model formulation

2.1. Piston excitation due to wave motion

The issue of wave hydrodynamics and their effects on floating structures is not trivial and has received significant attention in the literature [24,25], especially with reference to the control of point absorber WECs [26,27]. The scattering of an incident wave induces

vertical (heaving) buoy motion, which results in waves radiating away from the oscillating buoy; in turn, momentum changes in the surrounding fluid give rise to net forces acting on the buoy. When isolating a single floating member for analysis as we do in this work, we choose to neglect the effects of neighboring buoys to the wave motion, energy content and resulting forces. In this section, we present the equation of motion – including the effects of buoyancy, wave excitation and drag forces – for a single prismatic buoy connected to a piston via a rod or cable of known stiffness under the excitation of a simple harmonic wave. The proposed model utilizes numerical methods and can therefore be used to predict the system response to more complex wave profiles, which can be characterized a priori as time histories of wave surface displacement $z_w(t)$. Furthermore, the dynamic adaptation of wave energy content with energy extraction, which will affect downstream wave height, is not relevant for a single buoy and is neglected in the present model; however, this will be included in the future modeling of the MP^{2}PTO WEC that will utilize grids of buoys (a floater blanket).

Let an incident wave have a sinusoidal shape with its displacement about a zero mean, velocity and acceleration defined as

$$\begin{aligned} z_w &= -\frac{H_w}{2}\cos\left(\frac{2\pi}{T_w}t\right) \\ \dot{z}_w &= \frac{\pi H_w}{T_w}\sin\left(\frac{2\pi}{T_w}t\right) \\ \ddot{z}_w &= \frac{2\pi^2 H_w}{T_w^2}\cos\left(\frac{2\pi}{T_w}t\right) \end{aligned} \tag{1}$$

where H_w is the wave height and T_w is the wave period [24]. At any time instant, a prismatic buoy of mass m_b, height H_b and cross-sectional area A_b will have displacement z_b and will be submerged in the sea water by an amount D_b defined as

$$D_b = z_w - z_b + \frac{1}{2}H_b. \tag{2}$$

Consequently, the buoyancy force acting on it will be

$$F_b = \begin{cases} 0 & \text{if } D_b \le 0 \\ \rho_{sw} g A_b D_b & \text{if } 0 < D_b \le H_b \\ \rho_{sw} g A_b H_b & \text{if } D_b > H_b \end{cases} \tag{3}$$

where ρ_{sw} is the density of sea water and g is the gravitational constant. The buoyancy force will be constant for a fully-submerged buoy, zero if the buoy comes out of the sea water, and dependent on the magnitude of D_b otherwise.

When the buoy moves in stationary fluid, its acceleration induces the fluid in its immediate neighborhood to accelerate and this, in turn, induces an added mass effect onto the member [24]. This added mass can be described in terms of an added mass coefficient C_a [25],

$$m_a = \begin{cases} 0 & \text{if } D_b \le 0 \\ C_a \rho_{sw} A_b D_b & \text{if } 0 < D_b \le H_b \\ C_a \rho_{sw} A_b H_b & \text{if } D_b > H_b \end{cases} \tag{4}$$

and varies with the amount of submersion. Accounting for the added mass, the equation of motion of the buoy connected to a piston with relative displacement z and velocity $\dot{z}$ takes the following form:

$$\begin{aligned} &(m_a + m_b)\ddot{z}_b + B\dot{z}_b + C(\dot{z}_b - \dot{z}) + \rho_{sw} g A_b z_b + K(z_b - z) \\ &= -m_b g + F_b + F_d + F_e \end{aligned} \tag{5}$$

where $K(z_b - z) \equiv F_K$ and $C(\dot{z}_b - \dot{z}) \equiv F_C$ are the spring and damping forces representing the connecting rod (or cable) between the buoy and piston, while F_d and F_e represent the drag and excitation forces, respectively. The value of the damping ratio between the buoy and piston can be used to calculate the damping coefficient $C = 2\zeta\sqrt{K m_1 m_2/(m_1 + m_2)}$, with masses m_1 and m_2 defined in a later section (§2.4). The connecting rod/cable has area A_r, density ρ_r and elastic modulus E_r so that its stiffness can be expressed as $K = E_r A_r / L_r$ while its mass is $m_r = \rho_r A_r L_r$. The weight of the rod will be accounted for in the piston equation of motion.

The drag force resists the motion of the buoy and is a function of the buoy velocity and drag coefficient C_d:

$$F_d = -\frac{1}{2}\rho_{sw} A_b C_d \left|\dot{z}_b\right| \dot{z}_b. \tag{6}$$

Published data can be used to extract a steady drag coefficient C_{ds} for steady flow as a function of buoy geometry [25]. The drag coefficient C_d in Equation (6) is the product of this steady drag coefficient C_{ds} with an amplification factor quantifying the relative effect of inertial versus drag forces. In turn, the amplification factor is a function of the Keulegan-Carpenter number $KC = \dot{z}_{b,max} T_w / \sqrt{A_b}$ that depends on the maximum buoy velocity, the wave period and the width of the prismatic buoy. The KC-number for the proposed system will be in the range of $0 < KC < 10$, meaning that the drag coefficient can be several times larger than the one obtained from steady flow data [25]; however, we make the simplifying assumption that $C_d \approx C_{ds}$ and plan to investigate this issue via experimental and simulation studies in future work.

The excitation force of Equation (5) includes pressure, inertial and damping contributions:

$$F_e = (m_a \ddot{z}_w + B\dot{z}_w + \rho_{sw} g A_b z_w) e^{-k_w D_b} \tag{7}$$

where the buoy submersion has been defined in Equation (2) and the wave number is $k_w = 2\pi/\lambda_w$ for wave length λ_w [28]. For the purposes of the present work, and in the absence of relevant data, we assume that $B = 0$ in the current simulations. This is an important assumption since this damping coefficient will affect the dissipation of wave energy and, hence, the energy available for extraction. Preliminary investigations suggest that the magnitude of the wave damping coefficient is ~35×10^4 Ns/m for the prismatic buoys proposed in the mechanical design of the Ocean Grazer. Simulations adopting this value for the wave damping coefficient yield very comparable results to those reported herein for $B = 0$; hence, we chose to not include them in this report pending more accurate hydrodynamic analyses. Similarly to the drag coefficient issue, we plan to perform experimental and numerical work to characterize the damping response of the buoys to be used in the full system for various buoy designs. This information will be used in future iterations of the model.

It should be noted that the conditions where the buoy comes out of the sea water completely or is fully submerged do not occur in our simulation results; instead, the buoyancy and excitation forces continuously scale with the instantaneous submersion calculated from the imposed wave displacement and the buoy heave motion as defined in Equation (2).

2.2. Pumping force and working fluid conservation

Following the buoy displacement, a cylindrical piston of height H_p, radius R_p and mass m_p moves within a cylinder of effective

length L_c and cross-sectional area A_c to pump the working fluid of density ρ from a lower to an upper reservoir. The effective cylinder length is measured relative to the bottoms of the two reservoirs, as shown in Fig. 2. The piston is hollow so that the top piston surface separates the two control volumes of working fluid with heights L_{21} and L_{43}. The top piston surface comprises two flaps (e.g. of semi-circular shape) that can open and close passively with the flow. Check valves control the flow from the cylinder to each reservoir: during the upstroke, the piston flaps close and the check valves open, allowing working fluid to enter the cylinder from the lower reservoir and discharge into the upper; conversely, during the downstroke, both check valves are closed and the piston flaps open, allowing the piston to sink into the stationary fluid column. Flow within the cylinder of cross-sectional area A_c is channeled from and to the upper and lower reservoirs with cross-sectional areas A_U and A_L, respectively. The initial values of the hydraulic heads (fluid levels) within the reservoirs are denoted as L_U and L_L.

As an initial condition, let the piston center of mass (COM) be located at an initial height L_0 measured from the bottom of the lower reservoir: this location will correspond to the center of the piston stroke relative to the cylinder base and should therefore be larger than half of the wave amplitude. Since the top piston surface thickness is very small relative to the fluid column, it can be neglected in the definition of L_{21} and L_{43}. Then, the dynamically varying distance between points 4 and 3 (Fig. 2) is

$$L_{43} = (L_0 + L_{COM}) + z \tag{8}$$

where L_{COM} is the offset between the COM and the top surface of the piston. Similarly, the distance between points 2 and 1 is

$$L_{21} = (L_c - L_0 - L_{COM}) - z. \tag{9}$$

The magnitude of the force required to pump the fluid column of the upstroke, hereafter termed the pumping force, is

$$F_p = A_c(p_2 - p_3) \tag{10}$$

where points 2 and 3 correspond to the top and bottom surfaces of the piston flaps and the cylinder cross-sectional area, depending on the piston radius R_p and the piston-cylinder separation s, is

$$A_c = \pi(R_p + s)^2. \tag{11}$$

The flow rate of the piston pump is a function of piston velocity

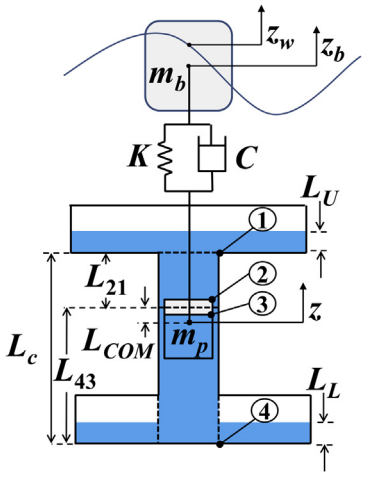

Fig. 2. Dynamical model of the single-piston pump (not showing the lateral piston displacement).

$v_z = \dot{z}$ so that

$$Q = A_c v_z = A_c \dot{z}. \tag{12}$$

Capacitance is derived from working fluid volume conservation and relates the pressure changes of the upper and lower reservoirs to hydraulic head fluctuations in each reservoir. Since flow rate is defined as the change in working fluid volume (area × height), the change in hydraulic head can be expressed as $\dot{H} = Q/A$, and the change in pressure at points 1 and 4 becomes

$$\begin{aligned} \dot{p}_1 &= \frac{\rho g}{A_U} Q = \frac{\rho g A_c}{A_U} \dot{z} \text{ and} \\ \dot{p}_4 &= -\frac{\rho g}{A_L} Q = -\frac{\rho g A_c}{A_L} \dot{z}. \end{aligned} \tag{13}$$

The change in the hydraulic head of the lower reservoir is negative as the working fluid flows from the lower to the upper reservoir during pumping. Integrating equation set (13) will yield the instantaneous values of the pressures at the upper and lower reservoir p_1 and p_4, respectively, which serve as state variables in the model.

Continuity in the working fluid system requires that the following equation holds:

$$p_1 - p_4 = p_{12} + p_{23} + p_{34} \tag{14}$$

so that the pressure gradient between points 2 and 3 can be expressed as

$$p_{23} = p_2 - p_3 = p_1 - p_4 + p_{21} + p_{43}. \tag{15}$$

The pressure gradients between points 2-1 and 4-3 can be calculated as functions of the inertance, which is a measure of the pressure difference required to cause a change in flow rate with time, and the dynamically varying head (neglecting losses due to wall friction, etc). Specifically, the pressure gradients are

$$\begin{aligned} p_{21} &= \frac{\rho(L_{21} + L_U)}{A_c} \dot{Q} + \rho L_{21} g \text{ and} \\ p_{43} &= \frac{\rho L_{43}}{A_c} \dot{Q} + \rho L_{43} g + \rho \dot{z}^2 \end{aligned} \tag{16}$$

with the change in flow rate calculated by differentiating Equation (12) with respect to time

$$\dot{Q} = A_c \ddot{z}, \tag{17}$$

the dynamically varying hydraulic head in the upper reservoir calculated as a function of the pressure at point 1, i.e. $L_U = p_1/\rho g$, and the term $\rho \dot{z}^2$ representing the change in momentum needed to accelerate the working fluid that enters the cylinder from the lower reservoir to attain the velocity of the moving fluid column. This formulation assumes that a check valve separates the working fluid volumes in the upper reservoir ($V_U = A_U L_U$) and the cylinder ($V_c = A_c L_c$) during the piston downstroke; however, this valve will open passively in the upstroke to accelerate the working fluid column whose total height becomes $L_{21}+L_U$. Since $p_{21} = p_2 - p_1 = p_2 - \rho L_U g$, the hydraulic head in the upper reservoir should not be included in the weight term $\rho L_{21} g$ because it occurs in the pressure difference term p_{21}. The relevant control volumes are shown in Fig. 2, where their boundaries are represented by dashed lines.

Combining the above formulae into the expression for the pumping force yields

$$F_p = A_c(p_1 - p_4) + \rho(L_{21} + L_U + L_{43})A_c\ddot{z} + \rho(L_{21} + L_{43})A_c g + \rho A_c \dot{z}^2 = -A_c p_4 + \underbrace{\rho(L_c + L_U)A_c}_{m_{f,nom}}(\ddot{z} + g) + \rho A_c \dot{z}^2 \quad (18)$$

where the second term includes the inertia and weight of the fluid column of nominal mass $m_{f,nom}$. It should be noted that cavitation is expected to occur for tall fluid columns. Placing the center of the piston stroke close to the bottom of the cylinder should reduce negative pressures during the upstroke: this is realized by appropriately selecting the value of L_0 to be small relative to the total cylinder length L_c but still larger than $H_w/2$. In addition, pressurization of the reservoirs, achieved by applying additional pressures p_L and p_H as parts of the initial conditions of the system, can also be used to avoid cavitation. Presently, we assume that $p_L = p_H = 0$.

The pumping force becomes zero during the downstroke for $v_z < 0$. This may introduce discontinuities to the system since the inertial term $m_{f,nom}(\ddot{z} + g)$ can be very large in the upstroke and results in an impact force (shock) acting on the piston during switching between the up- and downstrokes if this occurs instantaneously. In the present model, exponential growth and decay terms are introduced to the calculation of the fluid column mass m_f to compensate for this behavior:

$$m_f = \begin{cases} e^{G(t-t_{up})} & \text{in the upstroke} \\ m_{up,final}e^{-G(t-t_{up,final})} & \text{in the downstroke} \end{cases} \quad (19)$$

where G is a growth/decay factor, t_{up} denotes the starting time of the upstroke while $m_{up,final}$ and $t_{up,final}$ correspond to the fluid column mass and time instance at the last iteration of the upstroke, respectively. In addition, the value of m_f is bounded by 0 and the nominal value $m_{f,nom}$ defined as

$$m_{f,nom} = \rho(L_c + L_U)A_c \quad (20)$$

and derived in Equation (18). A more nuanced description could introduce a flow-dependent function for F_p that goes to zero more gradually as the piston flaps open incrementally in the downstroke based on predictions of their dynamic response. This, along with other issues such as the resistance of fluid flow within the cylinder due to wall friction, will be addressed in future work with the aid of computational fluid dynamics simulations. The authors have performed similar work that will be relevant to the unsteady flow in the section below the piston, in order to compute the exact velocity and pressure field and the minimum developed pressures [29,30].

2.3. Elastohydrodynamic lubrication at the piston-cylinder interface

Fig. 3 shows the side (a) and top views (b) of the piston-cylinder interface with the parameters relevant to the formulation of the elastohydrodynamic lubrication (EHL) problem [31]. For the purposes of this study, the tilting of the piston is only accounted for in the solution of the EHL problem and the tilting angle is assumed to be very small otherwise. The connecting cable or rod is attached at the piston COM, located at a distance L_{COM} below the top surface of the piston of radius R_p and height H_p. The piston is contained within a cylinder of radius R_p+s, where s is the separation between the piston and cylinder surfaces. Eccentricity e is defined as the radial offset between the COMs of the piston and cylinder. Assuming that the connecting cable/rod of length L_r can be represented as a straight line, an angle φ is formed between the tilted piston and the z-axis so that the eccentricity can be calculated as

$$e = L_r \sin\varphi \approx L_r\varphi \quad (21)$$

for very small values of φ. A cylindrical coordinate system (r,θ,z) with its origin at the piston COM is adopted for the solution of the EHL problem, as shown in Fig. 3. Taking advantage of axisymmetry, the corresponding Cartesian coordinate triad (x,y,z) can be rotated about the z-axis so that the eccentricity is always defined along the x-direction. Therefore, tilting of the connecting cable during the upstroke creates a wedge in the fluid film with the minimum film thickness occurring at the bottom and top of the piston during the up- and downstroke, respectively. The wedge effect results in the localized buildup of fluid film pressure that may induce elastic deformation in the surrounding solid surfaces [31]. For simplicity, and since piston tilting is accounted for in the EHL problem alone, EHL forces are applied at the piston COM so that moments about the y-axis are neglected in the formulation of the dynamical model. Indeed, while the maxima of the hydrodynamic forces are expected to occur around the location of the minimum film thickness, the film pressure is distributed over the piston surface so that the abovementioned assumption should hold for very small tilting angles.

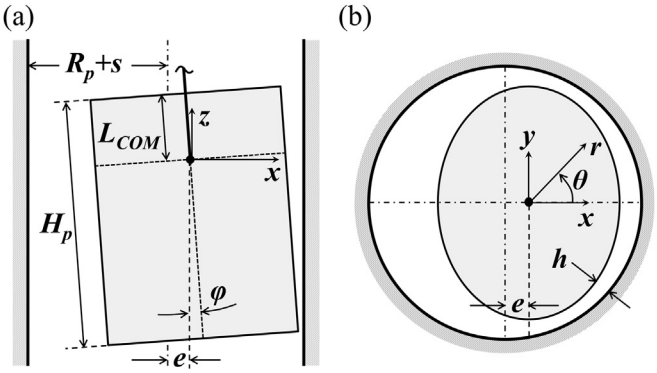

Fig. 3. The piston-cylinder interface side (a) and top views (b) with piston tilting as used in the EHL problem formulation.

Given that the origin is taken at the piston COM, the center of the cylinder can be thought of as being offset by an amount e in the negative x-direction for a positive (counterclockwise) tilting angle φ, defined in the third quadrant as shown in Fig. 3. Tilting also results in the shifting of the piston COM by an amount $\delta z = L_r(1-\cos\varphi)$; this can be neglected for a very small tilting angle since $\cos\varphi \approx 1$. The detailed formulation of the EHL problem, including the lubricating film thickness, can be found in Appendix 1.

The two-dimensional Reynolds equation in cylindrical coordinates, based on the incompressible and inviscid Navier-Stokes equations and the continuity condition [22,31],

$$\frac{\partial}{\partial z}\left(h^3\frac{\partial p}{\partial z}\right) + \frac{\partial}{R_p^2\partial\theta}\left(h^3\frac{\partial p}{\partial\theta}\right) = 6v_z\mu\frac{\partial h}{\partial z} \quad (22)$$

can be solved to yield the value of the film pressure $p(\theta,z)$. A full film is assumed to exist at all times within the radial clearance over the range of θ and the height of the piston. Fluid flow is assumed to be incompressible, inviscid with dynamic viscosity μ, and laminar since the piston-cylinder separation is significantly smaller than the piston dimensions, while pressure variation in the radial direction is neglected for the same reason. Piston velocity is calculated from the dynamical model (refer to Fig. 2) as $v_z = \dot{z}$. The following boundary conditions are assumed to hold:

$$p = p_2 \; at \; z = L_{COM}$$
$$p = p_3 \; at \; z = L_{COM} - H_p \tag{23}$$
$$\frac{\partial p}{\partial \theta} = 0 \; at \; \theta = \pi, \; -\pi$$

and are used to solve the Reynolds equation. In addition to the Neumann and Dirichlet boundary conditions specified in equation set (23), the Half-Sommerfeld boundary condition is also implemented whereby pressures smaller than the vapor pressure of the working fluid (absolute vapor pressure $p_v = 2.2\ kPa$ for an ISO Class HFC water-based hydraulic fluid at 20 °C) are set equal to the vapor pressure [31]. Nevertheless, cavitation does not appear in the simulation results due to the selected location of the piston stroke center close to the bottom of the cylinder.

The values of the pressures can be calculated from equation set (16) as functions of the state variables p_1 and p_4 during the upstroke:

$$p_2 = p_1 + \rho(L_{21} + L_U)\ddot{z} + \rho L_U \ddot{z} = \rho(L_{21} + L_U)(\ddot{z} + g) \text{ and}$$
$$p_3 = p_4 - \rho L_{43}(\ddot{z} + g) - \rho \dot{z}^2 - \frac{1}{2}\rho v_{leak}^2, \tag{24}$$

under the assumption that the piston height is much smaller than the cylinder height and including the effect of leakage through the piston-cylinder interface (note: $L_U = p_1/\rho g$). Instantaneous leakage is given by [22]

$$Q_{leak} = \int_{-\pi}^{\pi} \left(\frac{h v_z}{2} - \frac{h^3}{12\mu} \frac{\partial p}{\partial z} \right)_{z = L_{COM} - H_p} R_p d\theta, \tag{25}$$

and the corresponding leakage velocity is

$$v_{leak} = \frac{Q_{leak}}{A_c - A_p}. \tag{26}$$

During the downstroke, which occurs when the criterion $v_z < 0$ is satisfied, the pressures at the top and bottom of the piston flaps equalize. Flow into and out of the cylinder is inhibited by check valves; this is imposed by maintaining p_1 and p_4 constant, $Q = 0$ and setting the fluid column acceleration to zero. Hence, pressure at the instantaneous piston location can be calculated as:

$$p_2 = p_3 = \rho(L_{21} + L_U)g = \rho g(L_c - L_0 - L_{COM} - z + L_U). \tag{27}$$

EHL at the piston-cylinder interface will result in two fluid forces acting on the piston: a normal (bearing) force pushing the piston towards the center of the cylinder and a shear force resisting the vertical piston motion. These can be calculated using the following equations [22,32]:

$$F_n = \int_{L_{COM} - H_p}^{L_{COM}} \int_{-\pi}^{\pi} p \cos\theta \, R_p d\theta dz \; and \tag{28}$$

$$F_f = \int_{L_{COM} - H_p}^{L_{COM}} \int_{-\pi}^{\pi} \left(\frac{\mu v_z}{h} + \frac{h}{2} \frac{\partial p}{\partial z} \right) R_p d\theta dz. \tag{29}$$

A penalty method is used to account for solid contact whereby an elastic (Hertzian) restoring force is activated whenever the fluid film thickness becomes negative [33]:

$$F_r = \frac{4}{3} E^* R^{1/2} (s - x_L)^{3/2} \tag{30}$$

where $x_L = x + (H_p - L_{COM}) sin\varphi$ is the largest lateral displacement measured at the bottom of the tilted piston. In potential instances of solid contact, the film pressure and thickness distributions are maintained constant and equal to the last step where EHL existed. Again, the reader is referred to Appendix 1 for descriptions of the variables used in the EHL model.

2.4. Equations of motion for the full system

The buoy of mass m_b tracking the wave displacement z_w displays heaving motion z_b and actuates a piston with displacements x and z in the lateral and vertical directions respectively, as shown in Fig. 4 (also refer to Figs. 2 and 3). As stated previously, tilting of the piston is accounted for only in the solution of the EHL problem and is assumed to be negligible in the dynamics of the system (i.e. moments about the piston COM are neglected); however, the force acting to restore the piston COM to the center of the cylinder is accounted for. Displacements (DOFs) are measured relative to the COMs of the buoy and piston, respectively. Free body diagrams for the up- and downstroke are shown in Fig. 4: the pumping force is acting only during the upstroke and becomes zero otherwise.

In the case of the buoy (not shown in Fig. 4), the force balance in the vertical direction has been derived in a previous section. If we define an equivalent buoy mass

$$m_1 = m_b + m_a, \tag{31}$$

Equation (5) becomes

$$m_1 \ddot{z}_b + B\dot{z}_b + C(\dot{z}_b - \dot{z}) + \rho_{sw} g A_b z_b + K(z_b - z) = -m_b g + F_b + F_d + F_e. \tag{32}$$

Referring to the free body diagram of the piston in Fig. 4(a), the force balance in the vertical direction has the following form during the upstroke:

$$(m_r + m_p)\ddot{z} + C(\dot{z} - \dot{z}_b) + K(z - z_b) = -F_p - (m_r + m_p)g - F_f. \tag{33}$$

Introducing the pumping force of Equation (18) into the above expression yields:

$$\left(m_r + m_p + m_f\right)\ddot{z} + C(\dot{z} - \dot{z}_b) + K(z - z_b) = A_c p_4 - \left(m_r + m_p + m_f\right)g - \rho A_c \dot{z}^2 - F_f. \tag{34}$$

Let us define the equivalent mass m_2 in the following manner:

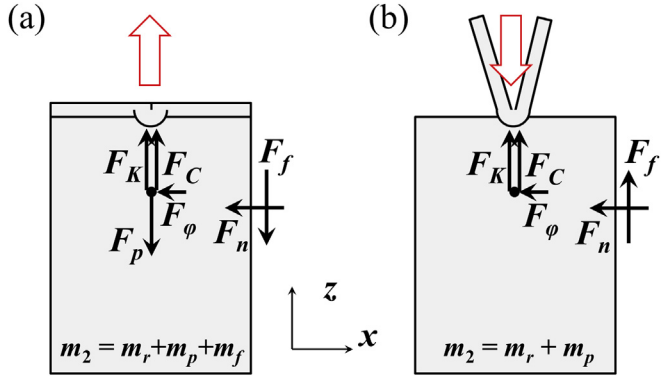

Fig. 4. Free body diagrams of the piston in the upstroke (a) and downstroke (b).

$$m_2 = \begin{cases} m_r + m_p + m_f & \text{in the upstroke} \\ m_r + m_p & \text{in the downstroke} \end{cases} \tag{35}$$

with the fluid column mass having been introduced in Equation (19). The equation of mass of the piston then becomes

$$m_2\ddot{z} + C(\dot{z} - \dot{z}_b) + K(z - z_b) = A_c p_4 - m_2 g - \rho A_c \dot{z}^2 - F_f \tag{36}$$

with the fluid mass m_f becoming zero and the pressures p_1 and p_4 being kept constant during the downstroke. The force F_f gives way to the solid friction force $\mu_{st}F_r$ in the case of solid contact.

The force balance equation in the lateral direction is

$$m_2\ddot{x} = -F_n - F_\varphi \tag{37}$$

where the normal force F_n acts during EHL and becomes the restoring force F_r in the eventuality of solid contact. The force acting to restore the piston COM to the cylinder center for a small (positive) tilting angle φ is

$$F_\varphi = \frac{m_2 g}{L_r} x \tag{38}$$

derived from the equations of motion of a pendulum. The force balance in the lateral direction can therefore be written as follows:

$$m_2\ddot{x} + m_2\frac{g}{L_r}x = -F_n. \tag{39}$$

In addition to Equations (31), (34) and (39), equation set (13) must be solved simultaneously to yield the instantaneous values of the pressures p_1 and p_4. In matrix form, the system equations follow the general form

$$\dot{\mathbf{q}} = \mathbf{A}\cdot\mathbf{q} + \mathbf{f} \tag{40}$$

where the state vector is

$$\mathbf{q} = \langle z_b \quad \dot{z}_b \quad z \quad \dot{z} \quad x \quad \dot{x} \quad p_1 \quad p_4 \rangle^T. \tag{41}$$

The matrix $\mathbf{A}$ is

$$\mathbf{A} = \begin{bmatrix} 0 & 1 & 0 & 0 & 0 & 0 & 0 & 0 \\ -\frac{(\rho_{sw} g A_b + K)}{m_1} & -\frac{(B+C)}{m_1} & \frac{K}{m_1} & \frac{C}{m_1} & 0 & 0 & 0 & 0 \\ 0 & 0 & 0 & 1 & 0 & 0 & 0 & 0 \\ \frac{K}{m_2} & \frac{C}{m_2} & -\frac{K}{m_2} & -\frac{C}{m_2} & 0 & 0 & 0 & A_c/m_2 \\ 0 & 0 & 0 & 0 & 0 & 1 & 0 & 0 \\ 0 & 0 & 0 & 0 & -g/L_r & 0 & 0 & 0 \\ 0 & 0 & 0 & \frac{\rho g A_c}{A_U} & 0 & 0 & 0 & 0 \\ 0 & 0 & 0 & -\frac{\rho g A_c}{A_L} & 0 & 0 & 0 & 0 \end{bmatrix} \tag{42}$$

and the forcing vector takes the following form:

$$\mathbf{f} = \begin{Bmatrix} 0 \\ -g\frac{m_b}{m_1} + \frac{F_b + F_d + F_e}{m_1} \\ 0 \\ -\frac{F_f - \mu_{st}F_r}{m_2} - g - \frac{\rho A_c \dot{z}^2}{m_2} \\ 0 \\ -\frac{F_n - F_r}{m_2} \\ 0 \\ 0 \end{Bmatrix} \tag{43}$$

where μ_{st} is the friction coefficient for steel-on-steel contact (assumed to be constant). Different materials and coatings are expected to be used in the actual system; hence, the friction coefficient will be different, while more accurate models of contact and friction can also be used without needing to define a friction coefficient a priori [34]. During the downstroke, check valves are activated to prevent backflow and the piston is allowed to sink passively into the working fluid column with open flaps. This is accounted for in the model by maintaining the pressures p_1 and p_4 constant and equal to the values attained at the last iteration of the upstroke.

The ODEs of Equation (40) are solved numerically using the Runge-Kutta-Fehlberg algorithm with adaptable step size [35]. The initial conditions of the state variables for the full system are

$$\mathbf{q}_0 = \begin{Bmatrix} z_{w,0} - \frac{m_{1,0} + m_{2,0}}{\rho_{sw} A_b} \\ 0 \\ z_{w,0} - \frac{m_{1,0} + m_{2,0}}{\rho_{sw} A_b} - \frac{(m_{1,0} + m_{2,0})g}{K} \\ 0 \\ 0 \\ 0 \\ \rho g L_{U,0} + p_H \\ \rho g L_{L,0} + p_L \end{Bmatrix} \tag{44}$$

based on the initial wave surface position $z_{w,0}$ with initial lower reservoir pressurizations $p_{H,L}$ and initial equivalent mass values of

$$m_{1,0} = m_b + C_a \rho_{sw} A_b (z_{w,0} + H_b/2),\ m_{f,0} = 0,\ \text{and}\\ m_{2,0} = m_r + m_p. \tag{45}$$

The initial displacements of the buoy and piston are calculated based on their equilibrium positions and accounting for the buoyancy force. It should be noted that the vertical displacements of the buoy and piston are expressed relative to a zero equilibrium position but will be separated by the connecting rod length L_r in the physical system.

3. Results and discussion

3.1. System parameters and assumptions

Simulations were performed for a single-piston pump with the resulting time histories of displacements, forces, flow-rates and pressures discussed in the following sections. Simulation parameters are summarized in Table 1.

Table 2 summarizes material and other constants, while Table 3 lists the parameters used in the generation of a harmonic wave. The working fluid is assumed to be a water-based hydraulic fluid (ISO Class HFC) at 20 °C and any temperature or pressure effects are neglected. Nevertheless, we can reasonably assume that the temperature would remain close to the nominal value (not necessarily 20 °C) due to the flooded conditions of operation. The average density of HFCs, adopted from the specifications given for HFC by Bosch Rexroth (document RE 90233, January 2015), is assumed to be 1.08 kg/cm^3, while the kinematic viscosity based on the ISO VG 68 specification is $\nu = 68\,cSt$; therefore, the absolute (dynamic) viscosity can be calculated to be $\mu = \rho\nu = 0.0734$ Pas. Such water-based hydraulic fluids (containing up to about 98% vol% water) have been shown to behave as Newtonian fluids [36], further suggesting that temperature or pressure effects can indeed be neglected. In comparison, water at 20 °C has the following properties: $\rho_w = 998$ kg/m^3, $\mu_w = 1.002$ mPas, and $p_{v,w} = 2.3$ kPa, i.e. its viscosity is roughly 70 times smaller than that of HFC. Water was used in additional simulations and juxtaposed with the HFC results, while a piston-cylinder separation $s = 100$ μm was selected to reduce volumetric leakage. Simulations performed with a commercial finite element solver (COMSOL Multiphysics software) have shown that, with water at 20 °C as a lubricant, the pumping efficiency decreases to below 90% when the piston-cylinder separation exceeds 250 μm, and becomes smaller than 20% for separations of 1 mm [23]; this is a result of the high volumetric leakage under high pressure differences that increases with increasing separation. The higher viscosity of HFC allows for larger piston-cylinder separations able to maintain a high pumping efficiency while simultaneously reducing the probability of solid contact, as will be discussed below.

The structural parameters of the buoy, connecting rod/cable, piston and reservoirs are listed in Table 4. Damping between the buoy and piston is characterized by the damping ratio that is arbitrarily assumed to have a value of 5%, while no initial pressurization was applied to the reservoirs since the pressure of the working fluid in the system never decreases below the relative vapor pressure.

Table 1
Simulation parameters.

Description	Symbol	Value	Unit
Duration	t_f	50	s
Minimum time step	Δt_{min}	5×10^{-6}	s
Integration tolerance	–	10^{-5}	–
Fluid column mass growth/decay rate	G	50	kg/s
EHL: number of grid points along z-dir.	N_z	10	–
EHL: number of grid points along è-dir.	N_θ	24	–
EHL: tolerance for convergence	–	1	Pa

Table 2
Constants.

Description	Symbol	Value	Unit
Gravitational constant	g	9.81	m/s
Sea water density	ρ_{sw}	1035	kg/m^3
Working fluid density (HFC at 20 °C)	ρ	1080	kg/m^3
Working fluid viscosity (HFC at 20 °C)	μ	0.0734	Pas
Work. fluid abs. vapor pr. (HFC at 20 °C)	p_v	2.2	kPa
Steel density	ρ_{st}	7850	kg/m^3
Steel Young's modulus	E_{st}	210	GPa
Steel Poisson ratio	ν_{st}	0.28	–
Steel-on-steel friction coefficient	μ_{st}	0.65	–

Table 3
Harmonic wave parameters.

Parameter	Symbol	Value	Unit
Wave height	H_w	4	m
Wave length	L_w	30	m
Wave period	T_w	10	s
Wave damping coefficient	B	0	Ns/m

3.2. Time histories of displacements, forces, flow-rates and pressures

Fig. 5 is a plot of the vertical (heave) displacement of the buoy for the harmonic wave input of Equation (1) over five wave periods. The initial transients corresponding to the first period (0–10 s) are the result of the initial conditions applied to the state variables during the numerical solution; these have been removed from the plots for clarity and, as a result, the time histories now span the range from 10 to 50 s. Even in the absence of wave damping ($B = 0$), the buoy is shown to smoothly track the wave motion after some initial transient. Nevertheless, an accurate characterization of this damping coefficient, possibly including linear and quadratic terms [25], will be necessary for the implementation of more complex wave profiles. The net vertical force acting on the buoy is given by

Table 4
Structural parameters.

Description	Symbol	Value	Unit
Buoy height	H_b	2	m
Buoy cross-sectional area	A_b	49	m^2
Buoy mass	m_b	1500	kg
Prismatic buoy added mass coefficient	C_A	0.9	–
Prismatic buoy steady drag coefficient	C_{ds}	1.5	–
Rod/cable radius	R_r	0.04	m
Rod/cable length	L_r	170	m
Rod/cable damping ratio	ζ	0.05	–
Piston height	H_p	0.1	m
Piston radius	R_p	0.1	m
Piston mass	m_p	150	kg
Piston-cylinder separation	s	400	μm
Initial piston-cylinder eccentricity	e	200	μm
Distance between points 1 and 4 (Fig. 2)	L_c	100	m
Distance between piston top and COM	L_{COM}	0.02	m
Piston center of stroke (initial location)	L_0	10	m
Upper reservoir cross-sectional area	A_U	49	m^2
Upper reservoir initial hydraulic head	L_U	10	m
Lower reservoir cross-sectional area	A_L	49	m^2
Lower reservoir initial hydraulic head	L_L	30	m
Reservoir initial pressurization	$p_{H,L}$	0	Pa

$$F_{buoy,net} = F_b + F_d + F_e \tag{46}$$

where the buoyancy, drag and excitation forces are defined in Equations (3), (6) and (7) and plotted in Fig. 5(b).

The net force acting on the buoy will be transmitted to the piston via the connecting rod/cable whose design will in turn affect the dynamic response of the piston. Piston velocity serves as the criterion for determining upward versus downward motion as shown in Fig. 6(b): $v_z > 0$ during the upstroke and $v_z < 0$ during the downstroke. As would be expected, this corresponds to changes in vertical piston motion as shown in Fig. 6(a) and denoted by the overlay plots of a 'switch' variable that becomes one during the upstroke and zero during the downstroke.

Switching between the up- and downstrokes gives rise to some higher-frequency oscillations observed in the velocity and shear force time histories plotted in Fig. 6(b–d), in addition to the plots of the 'switch' variable, due to the effect of the fluid column mass that goes from zero to several thousand kilograms or vice versa, resulting in an effective impact force acting on the piston at the instances of switching. Indeed, the frequency of these oscillations (~5.5 Hz) correlates well with the fundamental frequency of the connecting rod/cable $f = (1/2\pi)K/m_2$ during the downstroke (~4.8 Hz).

Water at 20 °C can initially maintain EHL at the piston-cylinder interface without solid contact, which begins with the second cycle, as shown in the insets of the shear and fluid bearing (normal) forces in Figs. 6(d) and 7(d); bouncing is observed inside the cylinder walls once solid contact is initiated. Since solid contact is expected to result in wear of the piston and cylinder surfaces, working fluid viscosity should be increased at the piston-cylinder interface in order to minimize solid contact. This is clearly shown in the main results of Figs. 6(a–c) and 7(a–c) pertaining to the HFC simulations: the pressure buildup in the lubricant is sufficient to separate the solid surfaces without solid contact, while the increased lubricant viscosity allows for a larger piston-cylinder separation ($s = 400$ μm for HFC compared to 100 μm required for pure water) that, in turn, further diminishes the probability of solid contact and wear at the interface.

The fluid forces exhibit 'jumps' at the switching instances, which can be explained by the instantaneous change in the boundary conditions of the EHL model: during the upstroke, a large pressure differential p_{23} is maintained at the piston-cylinder interface that goes to zero when the piston flaps open in the downstroke. As with the case of the fluid column mass, these artificial discontinuities will be removed in future iterations of the model by accounting for the dynamical behavior of the piston flaps. While most time histories presented in this paper, including that of the shear force in Fig. 6(c), are roughly periodic with the sinusoidal steady state having been reached by the second cycle, the time history of the normal (bearing) force in Fig. 7(c) is non-periodic: this partly arises from the fact that the pendular mass changes significantly between the up- and downstrokes, as captured in Equations (35) and (39), which in turn affects the oscillations in the x-direction. Since the shifting pendular frequency is not in phase with the heave motion, the result is non-periodic.

Another observation arising from Fig. 7(c) is the relatively small amplitude of the fluid bearing force F_n, which is defined in Equation (28) as the component of the radial force acting along the x-direction. Since the fluid film is assumed to exist within the entire piston-cylinder clearance, the magnitude of the normal force,

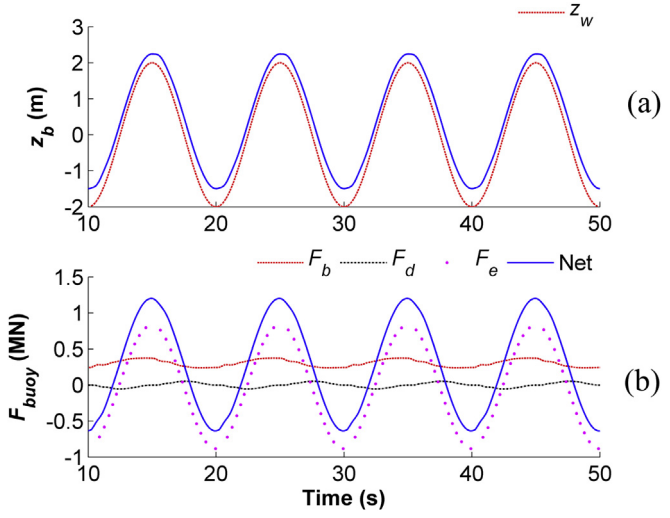

Fig. 5. Buoy/wave vertical displacements (a) and the forces acting on the buoy (b).

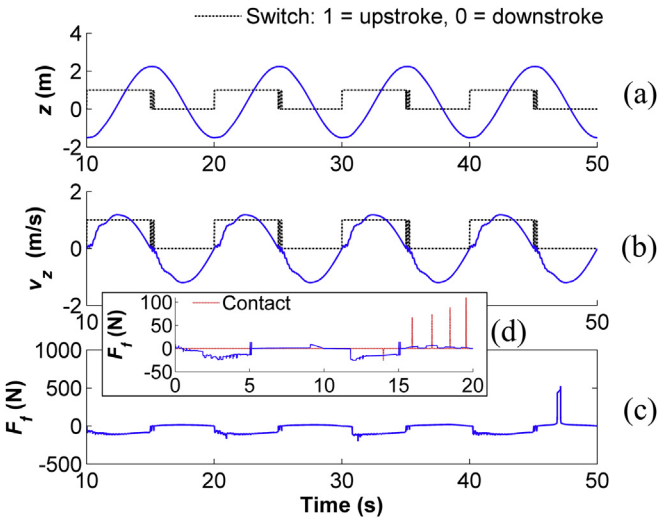

Fig. 6. Piston vertical displacement (a), velocity (b) and shear force acting at the piston-cylinder interface (c); inset (d) shows the shear and friction forces acting for the case when water at 20 °C is used as a lubricant (for s=100 μm).

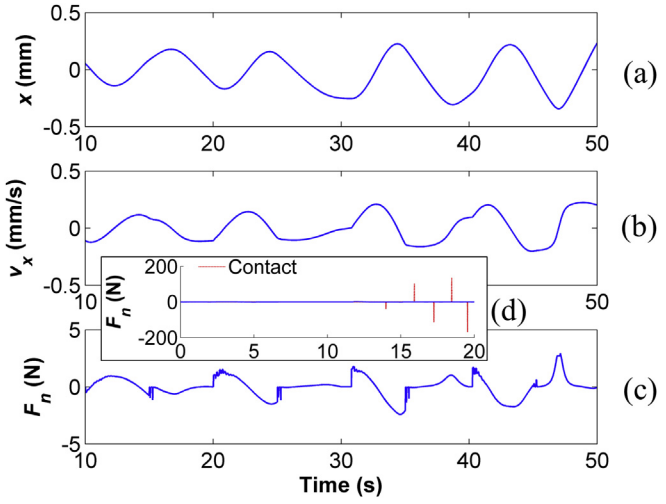

Fig. 7. Piston lateral displacement (a), velocity (b) and normal (bearing) force acting at the piston-cylinder interface (c); inset (d) shows the normal (bearing) and contact forces acting for the case when water at 20 °C is used as a lubricant.

which depends on the small difference in pressure between the positive and negative x-directions, results in a correspondingly small normal force. For example, when $x > 0$, integrating the pressure distribution over the 'positive' piston face ($-\pi/2 < \theta < \pi/2$) and taking the force component along the x-direction yields a net normal force that pushes the piston in the negative x-direction; doing the same for the pressure distribution along the 'negative' piston face yields a comparable force pushing the piston in the positive x-direction. The difference between these forces gives rise to a net normal force that has a comparatively smaller magnitude and opposes the direction of motion along the x-direction.

The piston displacement and velocity are plotted again in Fig. 8(a) to show that the higher-frequency vibrations in the velocity give rise to corresponding oscillations in the acceleration time history plotted in Fig. 8(b). Their amplitude is maximum at the switching instances as would be expected. The pumping force derived in Equation (18) comprises pressure-difference and inertial contributions and is nonzero only during the upstroke when the piston flaps remain closed. Introducing a nonzero wave damping coefficient B dampens some of the higher-frequency vibration content and allows for the acceleration to become almost zero at the top- and bottom-dead-centers of the piston oscillation; the same can be achieved in a more realistic manner by introducing the piston flap dynamics into the model. Consequently, the time histories of piston velocity and acceleration, along with the relevant forces such as the pumping force, would become smoother around switching instances. In the absence of the above, we utilize smoothing of the fluid column mass calculation to remove the detrimental effect of these non-physical higher-frequency vibrations from the simulation results (Fig. 9, below).

Furthermore, it can be observed that the magnitude of the pumping force is relatively small compared to the net force on the buoy (~30 *kN* compared to ~1 *MN*, respectively); however, while the order of magnitude of the net force on the buoy is expected to remain more or less constant, the pumping force can change significantly depending on the pumped volume. Specifically, it is straightforward to derive how scaling the piston radius by a factor X will scale the pumped volume by a factor X^2 and how, for example, a piston of twice the nominal radius will pump four times the working fluid volume increasing the pumping force to ~100 *kN*. For a multi-piston pump designed to employ three pistons with radii of $R_1 = 5$ *cm*, $R_2 = 2R_1 = 10$ cm and $R_3 = 2R_2 = 20$ cm simultaneously

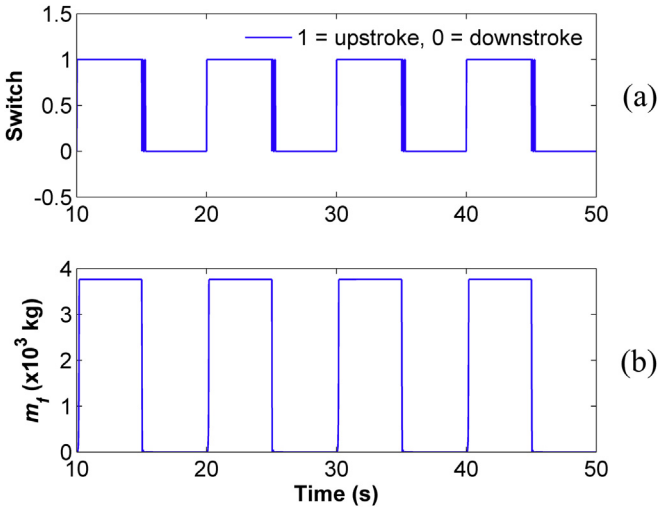

Fig. 9. Upstroke v. downstroke switching (a) and smoothing of the fluid column mass (b).

when very large waves come into the WEC, the total working fluid column volume would be ~$\sum X^2 = 0.5^2 + 1^2 + 2^2 = 5.25$ times the nominal volume and, correspondingly, the total pumping force would be ~525 kN with potential peaks at twice that magnitude during switching instances. Such forces would be sufficient to fully submerge the buoy, would alter the system's resonance and should, therefore, be accounted for in the MPP design; the latter lies outside the scope of the present work.

An exponential growth/decay function was introduced into the formulation of the fluid column mass as shown in Equations (19) and (20). Its effect is shown in Fig. 9: the switching between the upstroke and downstroke is done passively via the criterion of the piston velocity sign as shown in Fig. 6(a–b) and reproduced in Fig. 9(a) below.

The higher-frequency vibrations result in the rapid switching observed around seconds 15, 25, 25 and 45, and induce non-physical vibrations as discussed previously. By using the exponential growth/decay function, switching is assumed to take some amount of time δt that depends on the value of the growth/decay

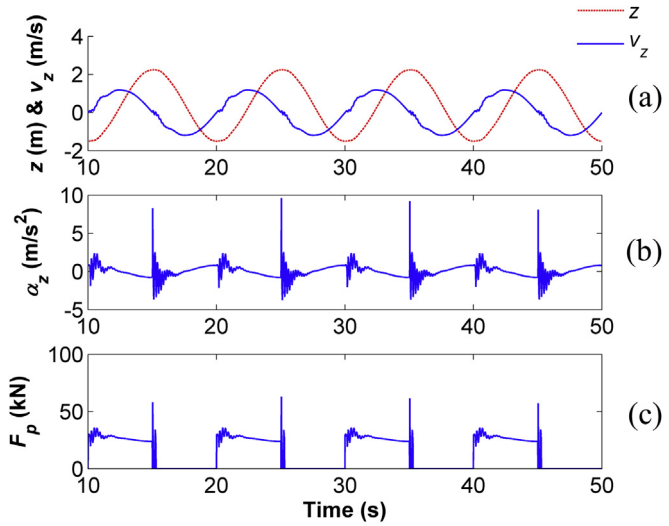

Fig. 8. Piston displacement and velocity (a), acceleration (b) and the pumping force (c).

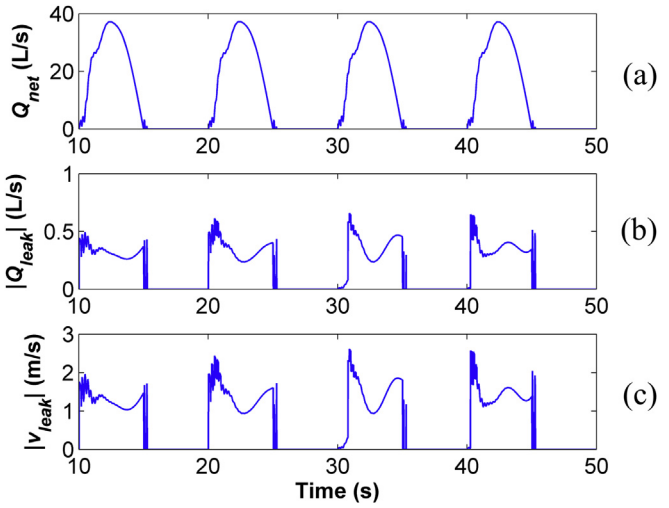

Fig. 10. Instantaneous flow rate (a), absolute leakage flow rate (b) and absolute leakage velocity (c).

rate and the nominal fluid column mass, rather than occurring instantaneously between iterations $i-1$ and i. For example, using a growth/decay rate of G=50 kg/s and nominal fluid column mass $m_{f,nom} \approx 3{,}500\,kg$, the fluid column mass goes from 0 to $m_{f,nom}$ or vice versa within

$$\delta t = \frac{ln\left(m_{f,nom}\right)}{G} \approx 0.16\,s. \tag{47}$$

This is shown in Fig. 9(b) where the behavior of m_f has been smoothed relative to the switching. In future work, we plan to investigate the dynamics of the piston flaps and remove artificial smoothing altogether.

The net instantaneous flow-rate of a single-piston pump is plotted in Fig. 10(a). As per the model formulation, the working fluid gets pumped to the upper reservoir only during the upstroke and the flow-rate becomes zero otherwise. The net flow-rate accounts for the leakage, given in Equation (25) and plotted in Fig. 10(b), which is ~1% of the gross value for the piston-cylinder clearance of 400 μm used in the simulations. This is given by

$$Q_{net} = A_c v_z - Q_{leak}. \tag{48}$$

Fig. 10(c) is a plot of the leakage velocity given in Equation (26) and provides an indication of the loss of pressure from the piston-cylinder separation. Leakage through the piston-cylinder clearance occurs during the upstroke when the positive leakage flow-rate is subtracted from $A_c v_z$ to yield Q_{net}. Volumetric leakage is very sensitive to viscosity. When using pure water, for example, its lower viscosity results in significant leakage for the same piston-cylinder separation of 400 μm; in order to reduce this to the levels achieved with an HFC lubricant, the separation must be reduced to 100 μm, which significantly increases the probability of solid contact (as shown in Figs. 6(d) and 7(d)).

The transfer of working fluid from the lower to the upper reservoir due to the pumping action of the reciprocating piston can be quantified as the change in pressures p_1 and p_4 as shown in Fig. 11(a–b). The instantaneous hydraulic head in each container can be calculated as the ratio of these pressures to the product of the working fluid density and the gravitational constant, i.e. $L_U = p_1/\rho g$ and $L_L = p_4/\rho g$, respectively. As would be expected, the

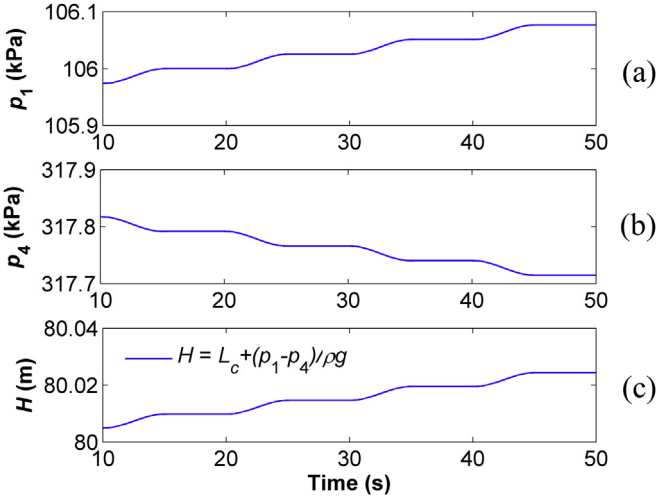

Fig. 11. Pressures in the upper (a) and lower reservoirs (b) and the (maximum) hydraulic head (c).

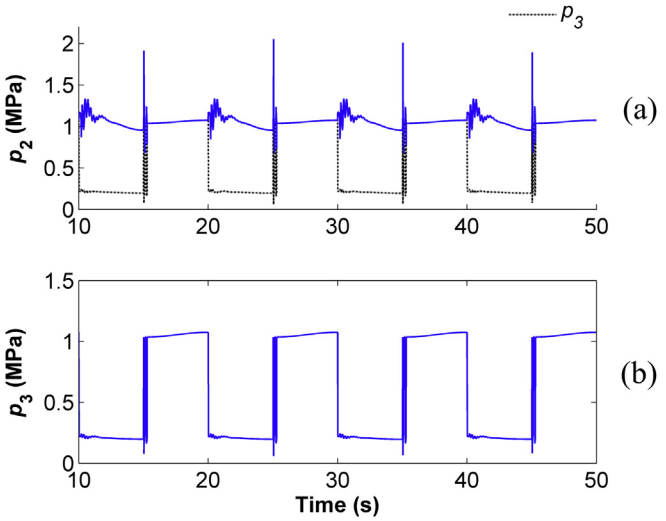

Fig. 12. Pressures above (a) and below (b) the piston flaps.

pressure (and head) increases in the upper reservoir and decreases in the lower by an amount corresponding to the volume of pumped working fluid. The maximum hydraulic head available for the turbine is plotted in Fig. 11(c) and includes the height difference between points 1 and 4 (refer to Fig. 2); this increases by roughly 5 mm per cycle.

The instantaneous pressures p_2 and p_3 above and below the piston flaps are plotted in Fig. 12. A large pressure difference p_{23} is developed almost instantaneously at the closing of the piston flaps, while the two pressures converge to a common value during the downstroke when the piston flaps open. The relevant formulations for these pressures are given in equation set (24) and Equation (27), while the effect of this instantaneous switching was discussed previously within the context of the boundary conditions used in the EHL model. Correspondingly, non-physical oscillations close to the switching instances can be removed in future models by accounting for the piston flap dynamics.

3.3. EHL pressure distribution at the piston-cylinder interface

Referring to the piston displacement time histories in the vertical and lateral directions, given in Figs. 5(b) and 7(a), respectively, we examine two instances of EHL pressure distributions corresponding to local maxima and minima of the lateral displacement.

The fluid film pressure distribution at the piston-cylinder interface exhibits localized pressure buildup, albeit of very small

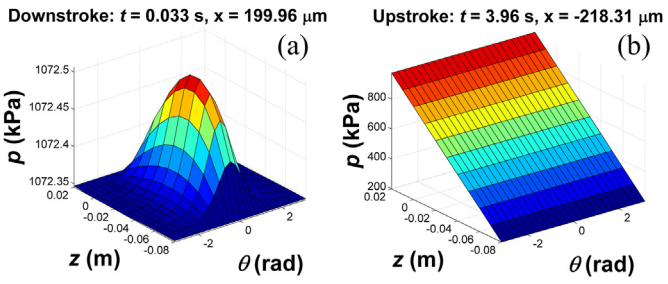

Fig. 13. Pressure distribution at the piston-cylinder interface during the downstroke (a) and upstroke (b).

magnitude (<150 Pa), as shown, for example, in the downstroke instance plotted in Fig. 13(a) and seen in similar numerical experiments [22]. Here, the pressure differential p_{23} is zero and p_2 and p_3 have converged to a value around 1072.35 kPa. By definition, the minimum film thickness and maximum film pressure will occur along the x-axis as this was defined in Fig. 3: for positive x, at $\theta = 0$ as is the case for the plotted instance, and for negative x at $\theta = \pm\pi$ (not shown).

During the upstroke, the inlet pressure is equal to p_2 and the outlet pressure, which never becomes smaller than the vapor pressure of water thereby avoiding cavitation, is equal to p_3 as per the boundary conditions of equation set (23). A pressure spike cannot be resolved in the plot of Fig. 13(b) due to the large pressure difference between the inlet and outlet conditions; this could presumably be achieved by using a much finer mesh for z and θ at immense computational cost.

As stated previously, the pressure buildup in the working fluid appears to be sufficient to provide bearing support for the normal forces developed during the lateral piston motion without leading to solid contact: this is the case when using HFC, but not when using pure water, and suggests that HFCs could successfully reduce wear. This behavior could be much more complex if viscous, thermal, transient and other effects were accounted for at the piston-cylinder interface. These will be investigated in subsequent models.

3.4. Power generation and loss

Power generation and loss in system components can be calculated over the duration of simulation time using the general formula $P = F \cdot v$. Hence, the net power of the buoy due to the buoyancy (3), drag (6) and excitation forces (7) can be found as follows:

$$P_{buoy} = (F_b + F_d + F_e)\dot{z}_b, \tag{49}$$

while the power corresponding to the spring (stiffness) and damping terms of the connecting rod is

$$\begin{aligned} P_{K,rod} &= K(z_b - z)(\dot{z}_b - \dot{z}) \text{ and} \\ P_{C,rod} &= -C(\dot{z}_b - \dot{z})(\dot{z}_b - \dot{z}) \end{aligned} \tag{50}$$

with the work or change in energy – defined as the integral of power over time – being conserved for the stiffness term but lost in the damping term. Additional power losses will occur at the piston-cylinder interface due to EHL (or solid contact and friction) forces and can be calculated as

$$P_{p-c} = \left(F_f + \mu_{st}F_r\right)\dot{z} + (F_n + F_r)\dot{x}. \tag{51}$$

The net power of the buoy fluctuates during the wave period with the power generated and lost, respectively, due to the buoyancy, drag and excitation components of the net buoy force as shown in Fig. 14(a). The current formulation of the excitation power affects the periodicity of the net power, whereas the buoyancy and drag powers show the same period as the excitation. In reality, significant buoy power will be lost due to the wave damping term of the excitation force but this is neglected in the present model ($B = 0$).

The wave energy flux for the waves under consideration (with significant wave height $H_{m,0} = H_w = 4$ m) can be calculated per meter of wave-front as $P_{wave} \cong 0.5{H_{m,0}}^2 T_w = 80\, kW/m$. For the width of the buoys $W_b = \sqrt{A_b} = 7$ m and the wave period $T_w = 10$ s, the total energy in the wave can be calculated as $E_{wave} = P_{wave}W_bT_w = 5600$ kJ. Out of this energy, only ~365 kJ are transferred to a single buoy (assuming zero wave damping), calculated as the integral of the net buoy power over one cycle: hence, the hydrodynamic efficiency of a single buoy is small at ~6.5%. The second buoy will extract energy from a smaller wave, the third one from an even smaller one, and so on as the wave energy is gradually absorbed by the device that will employ an array of adaptable pumps to maximize energy extraction. Returning to the considerations for a single buoy, in the limiting case where the total pumping force (including inertial and pressure difference contributions) will be equal to the total force that a buoy can support (~1 MN), then the total energy that could be extracted by each SPP would be roughly equal to the pumping efficiency times the buoy energy, i.e. $98.5\% \times 365\, kJ = 360$ kJ. Since it is undesirable to have a situation where the pumping force is close to the net force on the buoy, a larger number of pumps adapted to the incoming wave profile will be necessary to ensure that the buoy will always remain semi-submerged and operating optimally at resonance. Doing so will also require the use of robust control algorithms that will be investigated in future work together with physics-based characterizations of interactions between buoys.

Energy is transferred from the buoy to the piston via the connecting rod and from the lower to the upper reservoir via the working fluid. Even in the presence of buoy-piston damping, the energy in the rod is mostly conserved as shown in the power time history of Fig. 14(b–c) since $P_{C,rod}$ is small compared to $P_{K,rod}$. The power lost at the piston-cylinder interface due to EHL, plotted in Fig. 14(c), is similarly small. This power, which is zero around the switching instances, and the corresponding energy loss would be dissipated primarily as heat. Hence, an improved EHL formulation accounting for thermal effects becomes important for future work.

Pumping power is calculated as

$$P_{pumping} = F_p\dot{z} \tag{52}$$

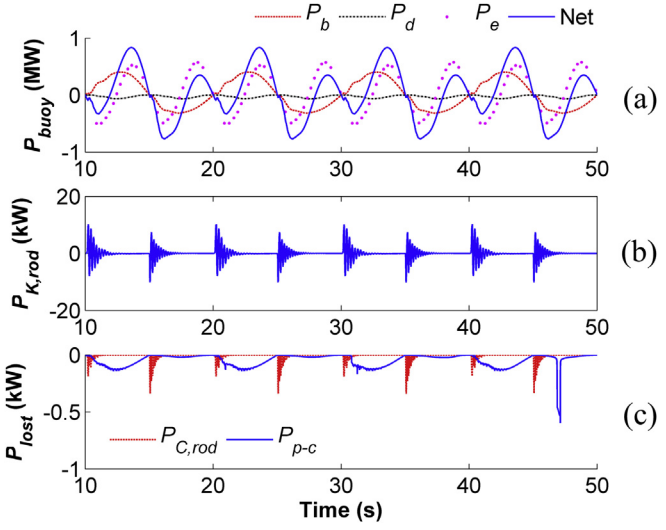

Fig. 14. Buoy power (a); rod spring power (b); lost power (c).

with the pumping force having been defined in Equation (18). The pumping energy (integral of the pumping power over time) is transferred via the working fluid and stored as potential energy. The potential power and energy are given in the following set of equations

$$P_{potential} = \rho g \overbrace{(L_c + L_U - L_L)}^{H} Q_{net}$$
$$Energy = \int_{t_i}^{t_f} P_{potential} dt \tag{53}$$

and are functions of the (maximum) dynamically varying hydraulic head H, shown schematically in Fig. 1(a), and the volume of working fluid pumped ($Q_{net} = \dot{V}_{net}$), with the net flow-rate having been defined in Equation (48).

The pumping and potential powers are close in amplitude, as shown in Fig. 15, with the deviation being attributable to the piston-cylinder interface (EHL) power loss plotted in Fig. 14(c) and the losses due to the transfer of momentum of the moving fluid column to the stationary fluid in the lower reservoir. The deviation between the corresponding pumping and potential energies (areas under the curves in Fig. 15) yields the efficiency of the pumping system

$$\eta_{pumping} = \frac{E_{potential}}{E_{pumping}} \times 100\%, \tag{54}$$

which is 98.5% for the current configuration with piston-cylinder separation $s = 400\,\mu m$, but without accounting for losses due to wall friction. To do so, we can employ the Darcy-Weisbach friction factor quantifying hydraulic loss due to wall friction that can be solved for in the laminar flow regime as $f_D = 64/Re$ and in the turbulent flow regime as

$$f_D = 0.25\left[\log_{10}\left(\frac{\varepsilon}{3.7D} + \frac{5.74}{Re^{0.9}}\right)\right]^{-2}, \tag{55}$$

which is an approximation for a full-flowing circular pipe, where the roughness is represented by the amplitude ε, D is the pipe diameter ($=2R_p+2s$), and Re is the Reynolds number. The Reynolds number can be calculated as $Re = \rho v_z D/\mu$ and ranges from ~1,470 for the smallest hydraulic cylinder diameter under consideration to ~5,885 for the largest (four times larger diameter), assuming a velocity of 1 m/s, as shown in Fig. 6(b). Correspondingly, the Darcy-Weisbach factor will vary between 0.044 for laminar flow and 0.036 for turbulent flow under the assumption of a (rather high) roughness amplitude $\varepsilon = 50\,\mu m$. The ratio of head loss to the length of the hydraulic cylinder will be

$$\frac{\Delta h}{L} = f_D \frac{1}{2g}\frac{v_z^2}{D}, \tag{56}$$

and its value is 0.022 for the laminar case and 0.0046 for the turbulent case for a moderate velocity of $v_z = 1$ m/s. In general, the influence of wall friction can be to reduce the mechanical efficiency due to hydraulic losses by as little as ~0.5% or as much as ~2.2% for the examined velocity.

It should be noted that these calculations assume that the cylinders span the entire height of the working fluid column (~200 m); however, this need not necessarily be the case, since the cylinders could be limited to the length of the expected maximum stroke (~12 m), and the remaining height could utilize ducts of larger diameters to transfer the fluid from the lower reservoir and into the upper one. This would result in a lower head loss Δh for the expanded duct sections due to their increased diameter (and Reynolds number) and reduced length, even though minor hydraulic losses would also be introduced due to flow expansions and constrictions. The general issue of hydraulic losses will be addressed in future pumping system designs and corresponding models.

We performed two additional simulations to investigate the effect of wave frequency on pumping behavior: one for short period waves ($T = 4$ s, $\lambda = 25$ m *and* $H = 1$ m) and one for long period waves ($T = 20$ s, $\lambda = 625\,m$ *and* $H = 6$ m). It should be noted that, while the connection between period and wave length is given in linear wave theory ($\lambda = gT^2/2\pi$), there is no clear relationship between the period and the wave height; hence, we arbitrarily chose the heights of 1 m and 6 m for these two simulations, respectively. We found that the energy extracted per cycle, as a representation of the hydraulic head added to the upper reservoir, scales roughly with the wave height: a 1-to-6 ratio of 25 kJ per cycle for 1 m-tall waves versus 157 kJ per cycle for 6 cm-tall waves. The mechanical efficiency remains comparable to that of the original case we studied at 98.6% and 97.4% for the short and long wave periods, respectively. Piston velocity was within the original envelope of ±1 m/s for the two simulations and, as a result, the peak values of the leakage flow rate and leakage velocity remained constant at around 0.5 L/s and 2 m/s, respectively. Hence, the volumetric efficiency also remains constant for longer wave periods, but will increase with increasing net flow rate for taller waves. These findings suggest that the system will work over the expected range of wave frequencies.

The efficiency calculations were validated by experimental measurements on an experimental prototype of the SPP where pure water at 20 °C was used as the lubricant [37,38]; these are summarized in Appendix 2. It was observed that the volumetric leakage occurring at the piston-cylinder separation is the main determinant of the pumping efficiency –itself a function of the mechanical and volumetric efficiencies of the pump–, which decreases to below 80% for separations larger than 200 μm. The same results were validated with finite element simulations (COMSOL Multiphysics software) [23] and point to target piston-cylinder

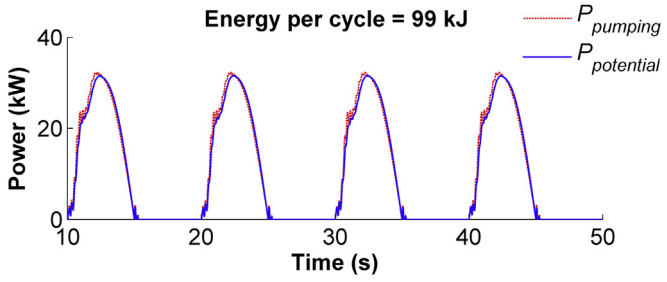

Fig. 15. Pumping versus potential power and energy generation per cycle.

separations around 100 μm when pure water is used as a lubricant. As stated previously, using a more viscous lubricant such as HFC allows for increasing separations while maintaining high efficiencies. It is expected that friction and lubrication at the valve interfaces will further reduce this efficiency, something that will be explored in future work.

The maximum instantaneous power that can be generated per cycle corresponds to the maximum hydraulic head available for the turbine and is found at the peak of the second upstroke (selected so as to avoid initial transients) at ~30 kW; correspondingly, the potential energy generated per cycle is 99 kJ for a single piston pump. Multiple pistons will scale up energy production for a single pump unit and will be able to adapt to the energy content of the wave, while this behavior is expected to improve accordingly for the MP^{2}PTO WEC. Overall, the use of multiple pump units is designed to incrementally extract almost all of the energy available in an incident wave and can transfer this energy to the stored working fluid with a high efficiency.

4. Conclusions

The mechanical design of the MP^{2}PTO WEC, together with a tribological model of a single-piston pump, have been presented for a novel renewable energy harvester termed the Ocean Grazer. The model accounts for the pump's dynamics, hydraulics and lubricated contact under a number of assumptions and gives estimates of the maximum potential energy gained per stroke. Within the full-scale Ocean Grazer system utilizing many such pumping units, this energy can be stored without losses and used, for example, to generate electricity on demand. EHL has been shown to dominate at the piston-cylinder interface, suggesting that water-based hydraulic fluids can potentially be used as a lubricants for this application with mechanical efficiencies close to 99%, and cavitation was avoided in the proposed pump design.

Future work, as summarized below, is necessary to relax the assumptions used in the present model:

- Investigation of wave damping and drag as a function of buoy design;
- EHL for pressure-dependent lubricant viscosity, thermal and transient effects;
- Improved formulation of piston flap and check valve dynamics to remove discontinuities;
- Calculation of the drag force acting on the piston while sinking into the water column;
- Inclusion of additional degrees of freedom for the buoy (e.g. downstream translation, roll) and piston (pitch), and accounting for deformations and the accurate characterization of damping in the connecting rod/cable;
- Investigation of tribology at secondary interfaces such as the rod/cable seals;
- Formulation of realistic wave displacement profiles accounting for the loss of energy content due to energy extraction for use with multiple buoys in a grid (floater blanket).

The present model will be used as a building block in the development of a multi-piston pump model coupled to variable-load control. A scale prototype of the multi-piston pump has been recently constructed and was used to validate model predictions: indeed, the reported mechanical efficiency of the system is close to 99%, with the pumping efficiency ($\eta_{pump} = \eta_{mech} \times \eta_{vol}$) being dominated by volumetric losses at critical interfaces. In turn, the resulting model can be used to optimize component and system design to increase power generation and reduce losses. In addition to parallel research activities in the hydrodynamic design of the buoy grid (floater blanket), and the floating structure, this work is fundamental in the realization of the Ocean Grazer and is a necessary tool in the performance of feasibility studies focusing on energetics, cost analyses, coupling to existing power grids, etc.

Acknowledgements

The authors would like to thank Wout Prins for useful discussions on the details behind the Ocean Grazer concept as well as Harmen Meijer, Marijn van Rooij and other students working on Ocean Grazer-related projects at the University of Groningen for their work.

Appendix 1. EHL model formulation and numerical solution

An analytical expression of the film thickness is necessary for the solution of the EHL problem. The parametric equations describing the cylinder and the piston, tilted about the y-axis, as shown in Fig. 3, are as follows:

$$\mathbf{r}_c = \begin{Bmatrix} (R_p + s)\cos\theta - L_r \sin\varphi \\ (R_p + s)\sin\theta \\ z \end{Bmatrix} \text{ and} \tag{A. 1}$$

$$\mathbf{r}_p = \mathbf{R}_y(\varphi)\cdot\mathbf{r}_{p,vertical} = \begin{bmatrix} cos\,\varphi & 0 & -sin\,\varphi \\ 0 & 1 & 0 \\ sin\,\varphi & 0 & cos\,\varphi \end{bmatrix} \begin{Bmatrix} R_p\,cos\,\theta \\ R_p\,sin\,\theta \\ z \end{Bmatrix} = \begin{Bmatrix} R_p\,cos\,\theta\,cos\,\varphi - z\,sin\,\varphi \\ R_p\,sin\,\theta \\ R_p\,cos\,\theta\,sin\,\varphi + z\,cos\,\varphi \end{Bmatrix}. \tag{A. 2}$$

The difference in the radial distance from the origin for the cylinder and piston respectively yields an analytical expression for the film thickness

$$\begin{aligned} h(\theta, z) &= w_r + (r_c - r_p) = w_r + \sqrt{x_c^2 + y_c^2} - \sqrt{x_p^2 + y_p^2} \\ &\approx w_r + \sqrt{(R_p + s)^2 + L_r\varphi\left[L_r\varphi - 2(R_p + s)cos\,\theta\right]} \\ &\quad - \sqrt{R_p^2 + z^2\varphi^2 - 2R_p z\varphi\,cos\,\theta} \end{aligned} \tag{A. 3}$$

where w_r denotes the deformation of the solid surfaces and $sin\varphi \approx \varphi$ and $cos\varphi \approx 1$ for a very small tilting angle, while $L_{COM} - H_p \le z \le L_{COM}$ and $-\pi \le \theta \le \pi$. The solid surfaces of the piston and cylinder will deform even at the lightest loads allowing for the fluid film to provide the essential bearing load capacity [31,33]. Assuming only elastic deformation, w_r must satisfy the following equation:

$$\frac{\partial w_r}{\partial z} = \frac{2}{\pi E^*} \int_{-\infty}^{+\infty} \frac{p(\zeta)}{z-\zeta} d\zeta \tag{A. 4}$$

where the ζ-coordinate lies in the direction of z and the combined elastic modulus is defined as

$$E^* = \left[\frac{1-\nu_1^2}{E_1} + \frac{1-\nu_2^2}{E_2} \right]^{-1}. \tag{A. 5}$$

Equation (A. 4) assumes smooth elastic surfaces. Roughness could potentially be incorporated in the prediction of the deformation utilizing multi-asperity [34,39–44] or fractal representations of surface roughness [45,46]. Similarly, finite element analysis could be used to predict the displacement fields of the piston and cylinder surfaces [22]. Given that the piston-cylinder separation will be larger in the proposed single-piston pump than in other applications such as reciprocal engines [20] and ring-less compressors [22], deformations are expected to remain within the elastic regime. Hence, Equation (22) is deemed sufficient as a first approximation of deformation in the EHL problem.

The Gauss-Seidel iteration method is used to solve the EHL problem [35]. The discretized form of the Reynolds Equation (22) becomeswhere the partial derivatives are defined as follows:

$$\frac{1}{\Delta z}\left(h_{i+\frac{1}{2}j}^3 \left.\frac{\partial p}{\partial z}\right|_{i+\frac{1}{2}j} - h_{i-\frac{1}{2}j}^3 \left.\frac{\partial p}{\partial z}\right|_{i-\frac{1}{2}j} \right) + \frac{1}{R_p^2 \Delta\theta}\left(h_{ij+\frac{1}{2}}^3 \left.\frac{\partial p}{\partial \theta}\right|_{ij+\frac{1}{2}} - h_{ij-\frac{1}{2}}^3 \left.\frac{\partial p}{\partial \theta}\right|_{ij-\frac{1}{2}} \right) = \frac{6\mu v_z}{\Delta z}\left(h_{i+\frac{1}{2}j} - h_{i-\frac{1}{2}j} \right) \tag{A. 6}$$

$$\begin{aligned}
\left.\frac{\partial p}{\partial z}\right|_{i+\frac{1}{2}j} &= \frac{1}{\Delta z}\left(p_{i+1j} - p_{ij}\right),\\
\left.\frac{\partial p}{\partial z}\right|_{i-\frac{1}{2}j} &= \frac{1}{\Delta z}\left(p_{ij} - p_{i-1j}\right),\\
\left.\frac{\partial p}{\partial \theta}\right|_{ij+\frac{1}{2}} &= \frac{1}{\Delta \theta}\left(p_{ij+1} - p_{ij}\right) \text{ and}\\
\left.\frac{\partial p}{\partial \theta}\right|_{ij-\frac{1}{2}} &= \frac{1}{\Delta \theta}\left(p_{ij} - p_{ij-1}\right)
\end{aligned} \tag{A. 7}$$

and the film thickness at the half steps can be calculated from Equation (A. 3) as

$$\begin{aligned}
h_{i+\frac{1}{2}j} &= \frac{1}{2}\left(h_{i+1j} + h_{ij}\right),\\
h_{i-\frac{1}{2}j} &= \frac{1}{2}\left(h_{ij} + h_{i-1j}\right),\\
h_{ij+\frac{1}{2}} &= \frac{1}{2}\left(h_{ij+1} + h_{ij}\right) \text{ and}\\
h_{ij-\frac{1}{2}} &= \frac{1}{2}\left(h_{ij} + h_{ij-1}\right)
\end{aligned} \tag{A. 8}$$

on a rectangular grid with step sizes Δz and $\Delta\theta$ along the azimuthal and angular directions, respectively. The local pressure at any grid point can be calculated from the previous iteration's grid point values using the following equation:

$$p_{ij} = \frac{\frac{6\mu v_z}{\Delta z}\left(h_{i-\frac{1}{2}j} + h_{i+\frac{1}{2}j}\right) + \frac{h_{i+\frac{1}{2}j}^3}{\Delta z^2} p_{i+1j} + \frac{h_{i-\frac{1}{2}j}^3}{\Delta z^2} p_{i-1j} + \frac{h_{ij+\frac{1}{2}}^3}{R_p^2 \Delta\theta^2} p_{ij+1} + \frac{h_{ij-\frac{1}{2}}^3}{R_p^2 \Delta\theta^2} p_{ij-1}}{\frac{h_{i+\frac{1}{2}j}^3}{\Delta z^2} + \frac{h_{i-\frac{1}{2}j}^3}{\Delta z^2} + \frac{h_{ij+\frac{1}{2}}^3}{R_p^2 \Delta\theta^2} + \frac{h_{ij-\frac{1}{2}}^3}{R_p^2 \Delta\theta^2}}. \tag{A. 9}$$

The nodal deformations are calculated using the parameterized form of Equation (A. 4):

$$w_{r_{ij}} = \frac{1}{2}\left(w_{r_{i+1j}} + w_{r_{i-1j}}\right) - \frac{\Delta z}{\pi E^*} \int_{-\infty}^{+\infty} \frac{p(\zeta)}{z-\zeta} d\zeta. \tag{A. 10}$$

The film thickness is updated by substituting the nodal deformations into Equation (A. 3) and the procedure is iterated until convergence is achieved in the film pressure distribution. This is achieved when the following criterion is satisfied [22]:

$$\sum_{i,j} p_{ij}^{(k)} - p_{ij}^{(k-1)} \le tolerance\ ,\ k = 1, 2, 3, \ldots \tag{A. 11}$$

where the convergence tolerance is defined in units of pressure (Pa) [20,22].

Appendix 2. Preliminary experimental validation of model predictions

A single-piston pump (SPP) Proof-of-Concept prototype was developed at the University of Groningen and was used to validate the predictions of a simplified dynamical model. Details on the

methods, as well as the experimental and simulation parameters used, can be found in the relevant conference paper [37], but representative results are provided here for completeness. It should be noted that pure water at 20 °C was used as a lubricant in, both, the experiments and simulations while the lubrication model was simplified with the use of hydrodynamic approximations for the normal and shear forces instead of the full EHL solutions discussed in the present paper.

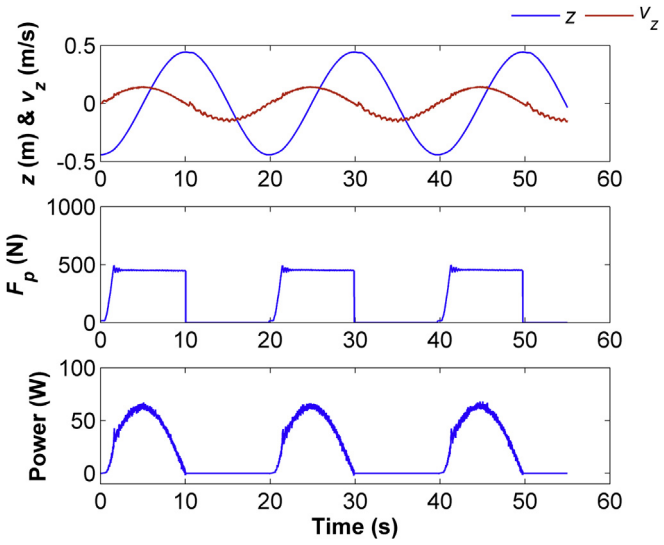

Fig. A1. Experimental measurements of kinematics (a); pumping force (b); and power production (c) [37].

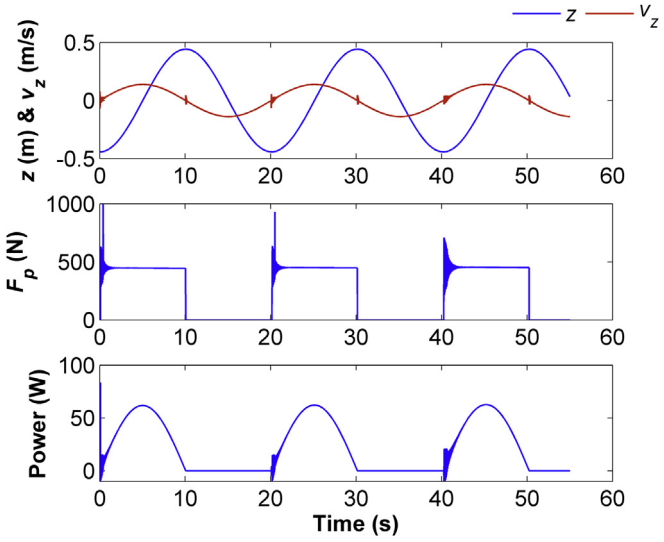

Fig. A2. Simulated predictions of kinematics (a); pumping force (b); and power production (c) [37].

Fig. A1(a) shows the kinematics of the SPP prototype: the displacement was measured with a displacement sensor (CELESCO SP1-50) and the velocity was calculated by numerically differentiating the displacement time history. The pumping force in Fig. A1(b) was measured with a force transducer (TEDEA HUNTLEIGH 615) installed at the cable connecting the piston to the actuating mechanical arm that was used to simulate sinusoidal wave motion, while the power production in Fig. A1(c) was calculated as the product of the pumping force and the velocity. The same results were predicted with the simplified SPP dynamical model whose parameters were modified to match the experimental conditions, as can be seen in Fig. A2. From the comparison of the two, it becomes clear that the oscillations observed at the switching instances of the simulated results are an artefact that must be corrected for in the dynamical contact models, as discussed in the body of the present paper: such oscillations might occur at the beginning of the downstroke, as can be seen in the experimental results, but their amplitude is small compared to that predicted in the simulations.

References

[1] R. Henderson, Design, simulation, and testing of a novel hydraulic power take-off system for the Pelamis wave energy converter, Renew. Energ 31 (2006) 271–283.
[2] B. Zanuttigh, E. Angelelli, M. Castagnetti, J.P. Kofoed, L. Martinelli, L. Clausen, The Wave Field around DEXA Devices and Implications for Coastal Protection, 2011.
[3] M. Kramer, L. Marquis, P. Frigaard, Performance Evaluation of the Wavestar Prototype, 2011.
[4] J.H. Norgaard, T.L. Andersen, Investigation of Wave Transmission from a Floating Wave Dragon Wave Energy Converter, 2012, pp. 509–516.
[5] SI-Ocean, Ocean Energy: State of the Art, 2012.
[6] W.A. Prins, Method and System for Extracting Kinetic Energy from Surface Waves of a Water, 2013. P101922PC00.
[7] A.I. Vakis, W. Prins, H. Meijer, First steps in the design and construction of the Ocean Grazer, in: ASME 2014 12th Biennial Conference on Engineering Systems Design and Analysis, 2014.
[8] J. Marti Saumell, Dynamical Modelling, Analysis and Control Design of a Distributed Sea Wave Energy Storage System. University of Groningen, 2013 (MSc Thesis).
[9] G. Li, M.R. Belmont, Model predictive control of sea wave energy converters – Part I: a convex approach for the case of a single device, Renew. Energ 69 (2014) 453–463.
[10] J.S. Anagnostopoulos, D.E. Papantonis, Pumping station design for a pumped-storage wind-hydro power plant, Energ Convers. Manage 48 (2007) 3009–3017.
[11] S. Saeid, R. Al-Khoury, H.M. Nick, M.A. Hicks, A prototype design model for deep low-enthalpy hydrothermal systems, Renew. Energ 77 (2015) 408–422.
[12] Y.T. Pei, X.L. Bui, J.P. van der Pal, D. Martinez-Martinez, X.B. Zhou, J. De Hosson, M. Th, Flexible diamond-like carbon films on rubber: on the origin of self-acting segmentation and film flexibility, Acta Mater 60 (2012) 5526–5535.
[13] L. Ma, C. Zhang, S. Liu, Progress in experimental study of aqueous lubrication, Chin. Sci. Bull. 57 (2012) 2062–2069.
[14] J.K. Lancaster, A review of the influence of environmental humidity and water on friction, lubrication and wear, Tribol. Int. 23 (1990) 371–389.
[15] J. Jia, J. Chen, H. Zhou, L. Hu, L. Chen, Comparative investigation on the wear and transfer behaviors of carbon fiber reinforced polymer composites under dry sliding and water lubrication, Compos Sci. Technol. 65 (2005) 1139–1147.
[16] Y. Yamamoto, T. Takashima, Friction and wear of water lubricated PEEK and PPS sliding contacts, Wear 253 (2002) 820–826.
[17] A. Mimaroglu, H. Unal, A. Ozel, Tribological performance of poly-etheretherketone and its composites under water environment, Macromol. Symp. 327 (2013) 108–113.
[18] X. Wang, K. Kato, K. Adachi, K. Aizawa, The effect of laser texturing of SiC surface on the critical load for the transition of water lubrication mode from hydrodynamic to mixed, Tribol. Int. 34 (2001) 703–711.
[19] M. Chen, K. Kato, K. Adachi, The comparisons of sliding speed and normal load effect on friction coefficients of self-mated Si3N4 and SiC under water lubrication, Tribol. Int. 35 (2002) 129–135.
[20] G.A. Livanos, N.P. Kyrtatos, Friction model of a marine diesel engine piston assembly, Tribol. Int. 40 (2007) 1441–1453.
[21] C. Cheng, Y. Yu, Numerical model for predicting thermodynamic cycle and thermal efficiency of a beta-type Stirling engine with rhombic-drive mechanism, Renew. Energ 35 (2010) 2590–2601.
[22] J.R. Cho, S.J. Moon, A numerical analysis of the interaction between the piston oil film and the component deformation in a reciprocating compressor, Tribol. Int. 38 (2005) 459–468.
[23] H. Meijer, Simulation of a Piston-type Hydraulic Pump for the Ocean Grazer. University of Groningen, 2014 (MSc Thesis).
[24] J. Falnes, Ocean Waves and Oscillating Systems, Cambridge University Press, 2002.
[25] Det Norske Veritas. Modelling and Analysis of Marine Operations, 2011.
[26] J. Falnes, J. Hals, Heaving buoys, point absorbers and arrays, Phil Trans. R. Soc. A 370 (2012) 246–277.
[27] E. Abraham, E.C. Kerrigan, Optimal active control and optimization of a wave energy converter, IEEE Trans. Sust. Energy 4 (2013) 324–332.
[28] C. Kourtzis, Numerical Modeling and Analysis of Operation and Energy Efficiency of a Non-piston Pumping Device for Wave-energy Extraction, Using a Buoyant Floating Submerged Vertical Pipe System. National Technical University of Athens (NTUA), 2013 (MSc Thesis).
[29] J. Anagnostopoulos, D.S. Mathioulakis, A flow study around a time-dependent 3-D asymmetric constriction, J. Fluids Struct. 19 (2004) 49–62.
[30] J.S. Anagnostopoulos, D.S. Mathioulakis, Unsteady flow field in a square tube

T-junction, Phys. Fluids 16 (2004) 3900–3910.
[31] J. Williams, Engineering Tribology, Cambridge University Press, 2005.
[32] M.M. Khonsari, E.R. Booser, Applied Tribology: Bearing Design and Lubrication, John Wiley & Sons, 2008.
[33] K.L. Johnson, Contact Mechanics, Cambridge University Press, Cambridge, UK, 1985.
[34] A.I. Vakis, Asperity interaction and substrate deformation in statistical summation models of contact between rough surfaces, J. Appl. Mech. 81 (2013) 41012.
[35] E. Kreyszig, Advanced Engineering Mathematics, eighth ed., John Wiley & Sons, 1999.
[36] O. Isaksson, Rheology for water-based hydraulic fluids, Wear 115 (1987) 3–17.
[37] M. van Rooij, H. Meijer, W.A. Prins, A.I. Vakis, Experimental performance evaluation and validation of dynamical contact models of the Ocean Grazer, OCEANS 2015-Genova (2015) 1–6.
[38] M. van Rooij, Experimental Validation of Dynamical Contact Models of the Ocean Grazer. University of Groningen, 2015 (MSc Thesis).
[39] J. Greenwood, J. Williamson, Contact of nominally flat surfaces, Proc. R. Soc. A 295 (1966) 300–319.
[40] W.R. Chang, I. Etsion, D.B. Bogy, An elastic-plastic model for the contact of rough surfaces, J. Tribol. 109 (1987) 257–263.
[41] L. Kogut, I. Etsion, A finite element based elastic-plastic model for the contact of rough surfaces, Tribol. Trans. 46 (2003) 383–390.
[42] A.Y. Suh, S. Lee, A.A. Polycarpou, Design optimization of ultra-low flying head-disk interfaces using an improved elastic-plastic rough surface model, J. Tribol. 128 (2006) 801–810.
[43] M. Ciavarella, J.A. Greenwood, M. Paggi, Inclusion of 'interaction' in the Greenwood and Williamson contact theory, Wear 265 (2008) 729–734.
[44] S. Chandrasekar, M. Eriten, A.A. Polycarpou, An improved model of asperity interaction in normal contact of rough surfaces, J. Appl. Mech. (2013) 80, 011025.
[45] W. Manners, J.A. Greenwood, Some observations on Persson's diffusion theory of elastic contact, Wear 261 (2006) 600–610.
[46] B.N.J. Persson, Relation between interfacial separation and load: a general theory of contact mechanics, Phys. Rev. Lett. 99 (2007) 125502.